RIS-Aided NLoS Monostatic Sensing Under Mobility and Angle-Doppler Coupling

N.B. When citing this work, cite the original published paper.

(article starts on next page)

RIS-Aided NLoS Monostatic Sensing under Mobility and Angle-Doppler Coupling

Mahmut Kemal Ercan[*], Musa Furkan Keskin[†], Sinan Gezici[*], and Henk Wymeersch[†]

[*] Department of Electrical and Electronics Engineering, Bilkent University, Turkey

[†] Department of Electrical Engineering, Chalmers University of Technology, Sweden

E-mail: ercan@ee.bilkent.edu.tr

Abstract—We investigate the problem of reconfigurable intelligent surface (RIS)-aided monostatic sensing of a mobile target under line-of-sight (LoS) blockage considering a single-antenna, full-duplex, and dual-functional radar-communications base station (BS). For the purpose of target detection and delay/Doppler/angle estimation, we derive a detector based on the generalized likelihood ratio test (GLRT), which entails a high-dimensional parameter search and leads to angle-Doppler coupling. To tackle these challenges, we propose a two-step algorithm for solving the GLRT detector/estimator in a low-complexity manner, accompanied by a RIS phase profile design tailored to circumvent the angle-Doppler coupling effect. Simulation results verify the effectiveness of the proposed algorithm, demonstrating its convergence to theoretical bounds and its superiority over state-of-the-art mobility-agnostic benchmarks.

Index Terms—Reconfigurable intelligent surfaces, monostatic sensing, non-line-of-sight (NLoS) sensing, angle-Doppler coupling.

I. INTRODUCTION

Reconfigurable intelligent surfaces (RISs) have emerged as a transformative technology towards 6G with the promise of significantly boosting communication rates and expanding coverage through the ability to overcome signal blockages, especially in mmWave and sub-THz systems [1]–[3]. RISs also have benefits to improve sensing capabilities [4], [5], thereby supporting integrated sensing and communications (ISAC) [6]–[8]. Applications include monostatic [9], bistatic [10] and multistatic [11] sensing, as well as simultaneous localization and mapping (SLAM) [12]. RIS-aided sensing brings several important advantages over conventional sensing without RIS, such as RIS phase profile design for illumination of desired sectors [13], [14], non-line-of-sight (NLoS) sensing in the presence of obstacles [15]–[17], signal-to-noise ratio (SNR) enhancement [18] and high-accuracy angle estimation via large aperture of RIS [19], [20].

In the context of RIS-aided sensing, several studies have focused on monostatic configurations [10], [15], [17], [20]–[23], particularly due to their attractive properties, including ease of synchronization and utilization of the entire signal (i.e., not only pilots). When the line-of-sight (LoS) path exists between the monostatic radar transceiver and the target, RIS can serve to boost the SNR via an extra, controlled path towards the target by judicious design of RIS element phases [18], [20], [23]. Under LoS blockage conditions (as shown in Fig. 1), RIS can act as an additional anchor to provide high-resolution angle-of-departure (AoD)/angle-of-arrival
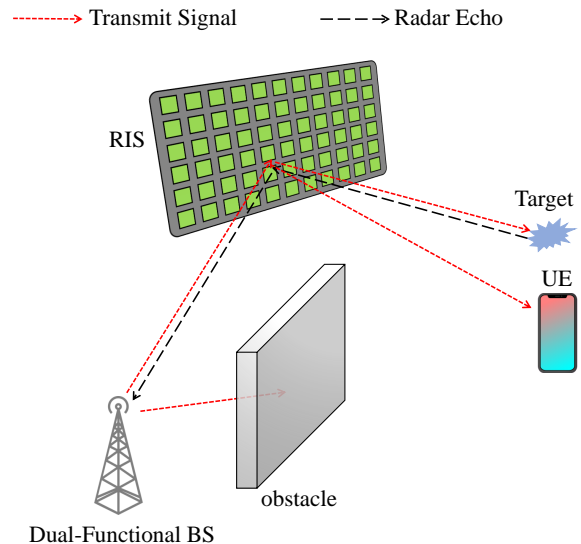
Fig. 1. RIS-aided monostatic sensing scenario under LoS blockage, where a dual-functional BS communicates with a user equipment (UE) in downlink (DL) while detecting a mobile target using the backscattered signals over the RIS path.

(AoA) measurements of potential targets [15], [24]. Given sufficient bandwidth (e.g., via orthogonal frequency-division multiplexing (OFDM) transmissions [25], [26]), the monostatic radar can combine angular information with round-trip delay measurements over the RIS-induced NLoS path to perform high-accuracy localization of targets in a surveillance area blocked by obstacles [17], [24].

A particular challenge arising in RIS-aided NLoS monostatic sensing pertains to detection and parameter estimation of *mobile targets*. In particular, target angle information can only be acquired through the RIS, which induces beamspace measurements at the radar receiver due to its passive nature (i.e., no sampling mechanism at the RIS), in turn requiring several non-parallel RIS beams [27]. In parallel, target Doppler is measured from slow-time phase shifts across transmissions. Consequently, the impact of mobility and RIS beam sweeping on slow-time phase shifts cannot be disentangled from each other, leading to the *angle-Doppler coupling* effect [28]. The few studies that considered RIS-aided sensing of mobile targets [16], [17], [22], [25], [26] focused mainly on RIS phase profile optimization and waveform design, omitting the algorithmic aspects. Hence, the two compelling problems remain unexplored in RIS-aided NLoS monostatic sensing research: *(i)* detection and four-dimensional (range-Doppler-azimuth-elevation) estimation of mobile targets, and *(ii)* the accompanying problem of angle-Doppler coupling.

In this paper, we tackle the problem of RIS-aided NLoS

monostatic sensing of a mobile target using the echoes of downlink signals transmitted by a dual-functional ISAC base station (BS). We derive the corresponding generalized likelihood ratio test (GLRT) detector, which involves computationally complex four-dimensional parameter search over range-Doppler-azimuth-elevation domains due to angle-Doppler coupling inherent to RIS-aided angle estimation under mobility. To address this challenge, we propose to employ repetitive RIS phase profiles and devise a novel low-complexity two-step estimator that exploits the proposed temporal design to circumvent the angle-Doppler coupling effect, enabling separate estimation of delay-Doppler and azimuth-elevation. Simulation results reveal the effectiveness of the proposed phase profile design and the low-complexity algorithm in mobile target sensing.

II. SYSTEM MODEL AND PROBLEM FORMULATION

In this section, we describe the RIS-aided NLoS sensing scenario, derive the signal model at the BS, and formulate the problem of detection/estimation of a mobile target.

A. Scenario

We consider the RIS-aided monostatic sensing scenario under LoS blockage as shown in Fig. 1, where a full-duplex dual-functional radar-communications BS with a known location performs monostatic sensing using the echoes of DL transmissions through the RIS-induced NLoS path [29], [30]. The aim is to detect a mobile target in the environment and estimate its parameters (delay, Doppler, angle). The BS is equipped with a single transmit (TX) and a single receive (RX) antenna, while the RIS has N_{RIS} elements. In addition, the RIS is assumed to have a known location and orientation.

B. Signal Model

For DL communications with a UE, the BS transmits an OFDM signal with N subcarriers and M symbols, with $x_{n,m}$ denoting the complex data/pilot on the nth subcarrier of the mth symbol. The subcarrier spacing and the symbol duration are defined as $\Delta_f = 1/T$ and $T_s = T + T_{\mathrm{cp}}$, respectively, with T denoting the elementary symbol duration and T_{cp} the cyclic prefix (CP) duration. We assume the existence of a single target in the environment. To prevent intersymbol interference (ISI), the CP duration is assumed to be larger than the round-trip delay of the target over the RIS path [31]–[34]. In this setup, the backscattered OFDM signal at the monostatic sensing receiver of the BS on the nth subcarrier of the mth symbol (after removing the CP and switching to frequency-domain) can be written as [15], [16]

$$y_{n,m} = \alpha \underbrace{\boldsymbol{a}^{\mathsf{T}}(\boldsymbol{\theta}^{\mathrm{br}})\boldsymbol{\Omega}_m\boldsymbol{a}(\boldsymbol{\theta})}_{\text{Target-RIS-BS path}} \underbrace{\boldsymbol{a}^{\mathsf{T}}(\boldsymbol{\theta})\boldsymbol{\Omega}_m\boldsymbol{a}(\boldsymbol{\theta}^{\mathrm{br}})}_{\text{BS-RIS-Target path}}$$
$$\times [\boldsymbol{c}(\tau)]_n[\boldsymbol{d}(\nu)]_m x_{n,m} + z_{n,m}, \quad (1)$$

where

- $\boldsymbol{\theta}^{\mathrm{br}} = [\theta_{\mathrm{az}}^{\mathrm{br}}, \theta_{\mathrm{el}}^{\mathrm{br}}]^{\mathsf{T}}$ is the known AoA from the BS to the RIS.
- $\boldsymbol{\theta} = [\theta_{\mathrm{az}}, \theta_{\mathrm{el}}]^{\mathsf{T}}$ is the AoD from the RIS to the target.
- α is the complex channel gain including the effects of *(i)* two-way attenuation over the forward BS-RIS-target path and the backward target-RIS-BS path, and *(ii)* radar-cross-

section (RCS) of the target, which can be calculated as [17]

$$|\alpha| = \sqrt{\frac{P_t G_b^2 G^2 F^2(\boldsymbol{\theta}) F^2(\boldsymbol{\theta}^{\mathrm{br}}) d_x^2 d_y^2 \lambda^2 \sigma_{\mathrm{RCS}}}{(4\pi)^5 d_{\mathrm{br}}^4 d^4}}. \quad (2)$$

Here, P_t is the transmit power, G_b is the BS antenna gain, G is the antenna power gain of an RIS patch, $F(\boldsymbol{\theta}) = (\cos\theta_{\mathrm{el}})^{0.285}$ is the normalized RIS power radiation pattern [35, Eq. (3)], d_x and d_y represent the RIS element spacing along the local horizontal and vertical axes, respectively, λ denotes the carrier wavelength, σ_{RCS} is the target RCS, and, d_{br} and d denote the BS-RIS and RIS-target distances, respectively.

- $\tau = 2(d_{\mathrm{br}} + d)/c$ and ν denote the round-trip delay and Doppler shift of the BS-RIS-target path, respectively, with c denoting the speed of propagation.
- $\boldsymbol{a}(\boldsymbol{\theta}) \in \mathbb{C}^{N_{\mathrm{RIS}} \times 1}$ denotes the array steering vector at the RIS, given as follows [36]:

$$[\boldsymbol{a}(\boldsymbol{\theta})]_i = e^{j\frac{2\pi}{\lambda}\cos\theta_{\mathrm{el}}(\cos\theta_{\mathrm{az}}p_{x,i}+\sin\theta_{\mathrm{az}}p_{y,i})}, \quad (3)$$

where $p_{x,i}$ and $p_{y,i}$ denote the position of the ith element in the horizontal and vertical axes of the RIS with respect to its center, respectively.

- $\boldsymbol{\Omega}_m = \mathrm{diag}(\boldsymbol{\omega}_m) \in \mathbb{C}^{N_{\mathrm{RIS}} \times N_{\mathrm{RIS}}}$ is the RIS phase profile for the mth symbol, containing RIS phase shifts $\boldsymbol{\omega}_m \in \mathbb{C}^{N_{\mathrm{RIS}} \times 1}$ on its diagonal.
- $\boldsymbol{c}(\tau) \in \mathbb{C}^{N \times 1}$ is the frequency-domain steering vector as a function of delay τ, given by

$$\boldsymbol{c}(\tau) = \left[1, \ e^{-j2\pi\Delta_f\tau}, \ \cdots, \ e^{-j2\pi(N-1)\Delta_f\tau}\right]^{\mathsf{T}}. \quad (4)$$

- $\boldsymbol{d}(\nu) \in \mathbb{C}^{M \times 1}$ is the time-domain steering vector as a function of Doppler ν, expressed as

$$\boldsymbol{d}(\nu) = \left[1, \ e^{j2\pi T_s\nu}, \ \cdots, \ e^{j2\pi(M-1)T_s\nu}\right]^{\mathsf{T}}. \quad (5)$$

- $z_{n,m} \sim \mathcal{CN}(0, N_0 N \Delta_f)$ is the additive complex Gaussian noise, with N_0 denoting the noise power spectral density (PSD).

To provide a more compact representation of (1), we define

$$\boldsymbol{b}(\boldsymbol{\theta}) \triangleq \boldsymbol{a}(\boldsymbol{\theta}) \odot \boldsymbol{a}(\boldsymbol{\theta}^{\mathrm{br}}) \in \mathbb{C}^{N_{\mathrm{RIS}} \times 1}, \quad (6)$$

where $\odot$ denotes the Hadamard (element-wise) product. Accordingly, we have

$$y_{n,m} = \alpha \left(\boldsymbol{b}^{\mathsf{T}}(\boldsymbol{\theta})\boldsymbol{\omega}_m\right)^2 [\boldsymbol{c}(\tau)]_n[\boldsymbol{d}(\nu)]_m x_{n,m} + z_{n,m}. \quad (7)$$

We further introduce the collection of RIS phase profiles

$$\boldsymbol{W} = [\boldsymbol{\omega}_0 \cdots \boldsymbol{\omega}_{M-1}] \in \mathbb{C}^{N_{\mathrm{RIS}} \times M}. \quad (8)$$

Using (8) and stacking over N subcarriers and M symbols, the model in (7) can be expressed in compact matrix form as

$$\boldsymbol{Y} = \boldsymbol{X} \odot \alpha\boldsymbol{c}(\tau)\left(\boldsymbol{d}^{\mathsf{T}}(\nu) \odot \boldsymbol{b}^{\mathsf{T}}(\boldsymbol{\theta})\boldsymbol{W} \odot \boldsymbol{b}^{\mathsf{T}}(\boldsymbol{\theta})\boldsymbol{W}\right) + \boldsymbol{Z}, \quad (9)$$

where $\boldsymbol{Y} \in \mathbb{C}^{N \times M}$ with $[\boldsymbol{Y}]_{n,m} = y_{n,m}$, $\boldsymbol{X} \in \mathbb{C}^{N \times M}$ with $[\boldsymbol{X}]_{n,m} = x_{n,m}$ and $\boldsymbol{Z} \in \mathbb{C}^{N \times M}$ is the additive noise matrix with $\mathrm{vec}(\boldsymbol{Z}) \sim \mathcal{CN}(\boldsymbol{0}, N_0 N \Delta_f \mathbf{I})$. For ease of exposition, we assume that all the symbols are 1, i.e., $\boldsymbol{X}$ is an all-one matrix. In this case, (9) becomes

$$\boldsymbol{Y} = \alpha\boldsymbol{c}(\tau)\left(\boldsymbol{d}^{\mathsf{T}}(\nu) \odot \boldsymbol{b}^{\mathsf{T}}(\boldsymbol{\theta})\boldsymbol{W} \odot \boldsymbol{b}^{\mathsf{T}}(\boldsymbol{\theta})\boldsymbol{W}\right) + \boldsymbol{Z}. \quad (10)$$

C. Problem Formulation

Given the frequency/slow-time observation matrix $\boldsymbol{Y}$ in (10), our goal is to detect the presence of the target and estimate its delay τ, Doppler ν and azimuth-elevation angles $\boldsymbol{\theta}$. Due to the angle-Doppler coupling over the slow-time domain (manifested through the terms $\boldsymbol{d}^{\mathsf{T}}(\nu)$ and $\boldsymbol{b}^{\mathsf{T}}(\boldsymbol{\theta})\boldsymbol{W}$), this poses a computationally complex problem. To tackle this challenge, in Sec. III we derive a generic GLRT detector and propose a tailor-made RIS phase profile design, along with a low-complexity detector/estimator, to resolve the angle-Doppler coupling.

III. Low-Complexity Detector/Estimator Design under Angle-Doppler Coupling

In this section, we first derive the GLRT detector for the sensing problem stated in Sec. II-C, which leads to a high-complexity optimization. Then, we propose a low-complexity two-step estimator that avoids high-dimensional parameter search in solving the GLRT, by exploiting the structure of a tailor-made RIS phase profile matrix $\boldsymbol{W}$ in (10).

A. GLRT Detector

To derive the GLRT detector, we re-cast (10) as

$$\boldsymbol{Y} = \overline{\boldsymbol{Y}}(\boldsymbol{\eta}) + \boldsymbol{Z} \in \mathbb{C}^{N \times M}, \tag{11}$$

where

$$\overline{\boldsymbol{Y}}(\boldsymbol{\eta}) \triangleq \alpha \boldsymbol{c}(\tau) \Big(\boldsymbol{d}^{\mathsf{T}}(\nu) \odot \boldsymbol{b}^{\mathsf{T}}(\boldsymbol{\theta})\boldsymbol{W} \odot \boldsymbol{b}^{\mathsf{T}}(\boldsymbol{\theta})\boldsymbol{W} \Big), \tag{12}$$

with $\boldsymbol{\eta} = [\alpha, \tau, \nu, \boldsymbol{\theta}]^{T}$ being the unknown parameter vector. Note that the RIS phase configuration matrix $\boldsymbol{W}$ is under our control; hence, we have degrees of freedom to design $\boldsymbol{W}$ according to our needs for radar detection and estimation. The hypothesis testing problem for the model in (11) can be formulated as

$$\boldsymbol{Y} = \begin{cases} \boldsymbol{Z}, & \text{under } \mathcal{H}_0 \\ \overline{\boldsymbol{Y}}(\boldsymbol{\eta}) + \boldsymbol{Z}, & \text{under } \mathcal{H}_1 \end{cases} \tag{13}$$

and the corresponding GLRT can be written as

$$\mathcal{L}(\boldsymbol{Y}) = \frac{\max_{\boldsymbol{\eta}} p_1(\boldsymbol{Y}|\boldsymbol{\eta})}{p_0(\boldsymbol{Y})} \underset{\mathcal{H}_0}{\overset{\mathcal{H}_1}{\gtrless}} \gamma \tag{14}$$

where γ is a threshold determined by a preset false alarm probability. In (14), the likelihood function for the no-target case $\mathcal{H}_0$ is given by

$$p_0(\boldsymbol{Y}) = \frac{1}{(\pi \sigma^2)^{MN}} \exp\left(-\frac{\|\boldsymbol{Y}\|_F^2}{2\sigma^2} \right), \tag{15}$$

where $\|\cdot\|_F$ denotes the Frobenius norm and $\sigma^2 = N_0 N \Delta_f$, while the likelihood function for the target-present case $\mathcal{H}_1$ is expressed as

$$p_1(\boldsymbol{Y}|\boldsymbol{\eta}) = \frac{1}{(\pi \sigma^2)^{MN}} \exp\left(-\frac{\|\boldsymbol{Y} - \overline{\boldsymbol{Y}}(\boldsymbol{\eta})\|_F^2}{2\sigma^2} \right). \tag{16}$$

Substituting (15) and (16) into (14) and simplifying, we obtain the log-likelihood ratio up to an additive and multiplicative constant as follows:

$$\mathcal{L}^{\log}(\boldsymbol{Y}) = \min_{\boldsymbol{\eta}} \|\boldsymbol{Y} - \overline{\boldsymbol{Y}}(\boldsymbol{\eta})\|_F^2 - \|\boldsymbol{Y}\|_F^2. \tag{17}$$

In (17), the optimal channel gain can be estimated in closed-form as a function of delay, Doppler and angle parameters [37]:

$$\widehat{\alpha} = \frac{\operatorname{tr}\left(\left(\boldsymbol{c}(\tau)\boldsymbol{h}^T(\nu, \boldsymbol{\theta}) \right)^H \boldsymbol{Y} \right)}{\|\boldsymbol{c}(\tau)\boldsymbol{h}^T(\nu, \boldsymbol{\theta})\|_F^2}, \tag{18}$$

where

$$\boldsymbol{h}(\nu, \boldsymbol{\theta}) \triangleq \boldsymbol{d}(\nu) \odot \boldsymbol{W}^T \boldsymbol{b}(\boldsymbol{\theta}) \odot \boldsymbol{W}^T \boldsymbol{b}(\boldsymbol{\theta}). \tag{19}$$

Plugging (18) into (17) yields

$$\mathcal{L}^{\log}(\boldsymbol{Y}) = \min_{\tau, \nu, \boldsymbol{\theta}} \left\| \boldsymbol{Y} - \frac{\operatorname{tr}\left(\left(\boldsymbol{c}(\tau)\boldsymbol{h}^T(\nu, \boldsymbol{\theta}) \right)^H \boldsymbol{Y} \right)}{\|\boldsymbol{c}(\tau)\boldsymbol{h}^T(\nu, \boldsymbol{\theta})\|_F} \boldsymbol{c}(\tau)\boldsymbol{h}^T(\nu, \boldsymbol{\theta}) \right\|_F^2 - \|\boldsymbol{Y}\|_F^2, \tag{20}$$

which can be simplified into (up to additive constants)

$$\mathcal{L}^{\log}(\boldsymbol{Y}) = \max_{\tau, \nu, \boldsymbol{\theta}} \frac{\left| \boldsymbol{c}^{\mathsf{H}}(\tau)\boldsymbol{Y}\boldsymbol{h}^*(\nu, \boldsymbol{\theta}) \right|^2}{\|\boldsymbol{h}(\nu, \boldsymbol{\theta})\|^2}. \tag{21}$$

In general, no further simplification is possible; hence, a 4D search is needed to estimate delay, Doppler, and 2D angle.

B. Low-Complexity Estimator

To avoid the 4D search, we harness the possibility of designing the RIS phase profile $\boldsymbol{W}$ in (12). With the proposed design, the observation model can be expressed in a form that allows disentangling angle-Doppler coupling. Then, the delay-Doppler estimation is described, followed by 2D angle processing. Finally, a refinement of the estimates and target detection are presented.

1) Repetitive RIS Phase Profile Design

The RIS phase profile is adjusted at each symbol duration:

$$\boldsymbol{W} = [\boldsymbol{\omega}_0 \cdots \boldsymbol{\omega}_{M-1}] \in \mathbb{C}^{N_{\mathrm{RIS}} \times M}, \tag{22}$$

$$\boldsymbol{b}^{\mathsf{T}}(\boldsymbol{\theta})\boldsymbol{W} = [\boldsymbol{b}^{\mathsf{T}}(\boldsymbol{\theta})\boldsymbol{\omega}_0 \cdots \boldsymbol{b}^{\mathsf{T}}(\boldsymbol{\theta})\boldsymbol{\omega}_{M-1}] \in \mathbb{C}^{1 \times M}. \tag{23}$$

From (12), we can see that the time-domain part of the signal depends on $\boldsymbol{d}(\nu)$ and $\boldsymbol{b}^{\mathsf{T}}(\boldsymbol{\theta})\boldsymbol{W}$. We will try to eliminate the effects of coupling between $\boldsymbol{\theta}$ and ν. To this end, we can repeat RIS profiles consecutively. In that case, we use L profiles and repeat each phase profile M/L times:

$$\underbrace{\boldsymbol{\omega}_1 \boldsymbol{\omega}_1 \ldots \boldsymbol{\omega}_1}_{M/L \text{ times}} \underbrace{\boldsymbol{\omega}_2 \boldsymbol{\omega}_2 \ldots \boldsymbol{\omega}_2}_{M/L \text{ times}} \cdots \underbrace{\boldsymbol{\omega}_L \ldots \boldsymbol{\omega}_L}_{M/L \text{ times}}. \tag{24}$$

With this design, during each time interval (i.e., M/L times), the phase shift caused by the angles is constant since the RIS profile is constant. Hence, we can eliminate the coupling effect during each time interval.

2) Observation Model with Repetitive RIS Phase Profiles

We will again use the signal model given in (12). But, to exploit the repetitive RIS phase profile on parameter estimation, we will use another form of (12) For that reason, we define

$$\boldsymbol{g}^{\mathsf{T}}(\boldsymbol{\theta}) = \boldsymbol{b}^{\mathsf{T}}(\boldsymbol{\theta})\boldsymbol{W} \odot \boldsymbol{b}^{\mathsf{T}}(\boldsymbol{\theta})\boldsymbol{W}, \tag{25}$$

leading to

$$\boldsymbol{Y} = \alpha \boldsymbol{c}(\tau)(\boldsymbol{d}^{\mathsf{T}}(\nu) \odot \boldsymbol{g}^{\mathsf{T}}(\boldsymbol{\theta})) + \boldsymbol{Z}. \tag{26}$$

Using the RIS phase profile with repetition, we can rewrite $\boldsymbol{g}^{\mathsf{T}}(\boldsymbol{\theta})$ as

$$\boldsymbol{g}^{\mathsf{T}}(\boldsymbol{\theta}) = \underbrace{(\boldsymbol{b}^{\mathsf{T}}(\boldsymbol{\theta})[\boldsymbol{\omega}_1 \ldots \boldsymbol{\omega}_L])^2}_{\triangleq \boldsymbol{g}_L^{\mathsf{T}}(\boldsymbol{\theta}) \in \mathbb{C}^{1 \times L}} \otimes \mathbf{1}_{M/L}^{\mathsf{T}} . \quad (27)$$

Therefore,

$$\boldsymbol{Y} = \alpha \boldsymbol{c}(\tau)[\boldsymbol{d}^{\mathsf{T}}(\nu) \odot (\boldsymbol{g}_L^{\mathsf{T}}(\boldsymbol{\theta}) \otimes \mathbf{1}_{M/L}^{\mathsf{T}})] + \boldsymbol{Z} . \quad (28)$$

Next, we define

$$\boldsymbol{d}_{M/L}(\nu) \triangleq [1\, e^{j2\pi\nu T_s} \ldots e^{j2\pi\nu(M/L-1)T_s}]^{\mathsf{T}} \in \mathbb{C}^{M/L \times 1}$$
$$\boldsymbol{d}_L(\nu) \triangleq [1\, e^{j2\pi\nu \frac{M}{L} T_s} \ldots e^{j2\pi\nu \frac{M}{L}(L-1)T_s}]^{\mathsf{T}} \in \mathbb{C}^{L \times 1},$$

which allows us to write

$$\boldsymbol{d}(\nu) = \boldsymbol{d}_L(\nu) \otimes \boldsymbol{d}_{M/L}(\nu) . \quad (29)$$

Plugging (29) into (28) yields

$$\begin{aligned}
\boldsymbol{Y} &= \alpha \boldsymbol{c}(\tau) \left[(\boldsymbol{g}_L(\boldsymbol{\theta}) \otimes \mathbf{1}_{M/L}) \odot (\boldsymbol{d}_L(\nu) \otimes \boldsymbol{d}_{M/L}(\nu)) \right]^{\mathsf{T}} + \boldsymbol{Z}, \\
&= \alpha \boldsymbol{c}(\tau) \left[(\boldsymbol{g}_L(\boldsymbol{\theta}) \odot \boldsymbol{d}_L(\nu)) \otimes (\mathbf{1}_{M/L} \odot \boldsymbol{d}_{M/L}(\nu)) \right]^{\mathsf{T}} + \boldsymbol{Z}, \\
&= \alpha \boldsymbol{c}(\tau) \left[(\boldsymbol{g}_L(\boldsymbol{\theta}) \odot \boldsymbol{d}_L(\nu)) \otimes (\boldsymbol{d}_{M/L}(\nu)) \right]^{\mathsf{T}} + \boldsymbol{Z} . \quad (30)
\end{aligned}$$

With this, we are now ready to introduce $\boldsymbol{\beta} \triangleq \alpha \boldsymbol{g}_L(\boldsymbol{\theta}) \odot \boldsymbol{d}_L(\nu) \in \mathbb{C}^{L \times 1}$, which will be a key to break down the 4D problem. With $\boldsymbol{\beta}$, we have that

$$\boldsymbol{Y} = \alpha \boldsymbol{c}(\tau) (\boldsymbol{\beta} \otimes \boldsymbol{d}_{M/L}(\nu))^{\mathsf{T}} + \boldsymbol{Z}. \quad (31)$$

By breaking up $\boldsymbol{Y} = [\boldsymbol{Y}_1 \cdots \boldsymbol{Y}_L]$, we have that $\boldsymbol{Y}_l = \beta_l \boldsymbol{c}(\tau) \boldsymbol{d}_{M/L}^{\mathsf{T}}(\nu) + \boldsymbol{Z}_l \in \mathbb{C}^{N \times M/L}$, $l = 1, \ldots, L$.

3) Delay-Doppler Estimation

We estimate τ and ν from $\{\boldsymbol{Y}_l\}_{l=1}^L$ by treating $\boldsymbol{\beta} = [\beta_1, \ldots, \beta_L]^{\mathsf{T}}$ as nuisance parameters. Due to the independence of noise across l, the maximum-likelihood (ML) estimator is expressed as

$$\min_{\tau, \nu, \boldsymbol{\beta}} \sum_{l=1}^L \| \boldsymbol{Y}_l - \beta_l \boldsymbol{c}(\tau) \boldsymbol{d}_{M/L}^{\mathsf{T}}(\nu) \|_F^2 . \quad (32)$$

Here, $\boldsymbol{\beta}$ can be obtained in closed form as a function of τ and ν, leading to

$$(\widehat{\tau}, \widehat{\nu}) = \arg\max_{\tau, \nu} \sum_{l=1}^L \left| \boldsymbol{c}^{\mathsf{H}}(\tau) \boldsymbol{Y}_l \boldsymbol{d}_{M/L}^*(\nu) \right|^2 . \quad (33)$$

For a fast implementation of (33), we can first obtain a coarse estimate and then refine it via gradient ascent. To obtain the coarse estimate, we can evaluate the objective function in (33) by performing IFFT over the frequency domain and FFT over the time domain for each $\boldsymbol{Y}_l$, and integrating non-coherently across l, which can be written as $\boldsymbol{Y}_{\tau,\nu} = \sum_{l=1}^L |\text{FFT}(\text{IFFT}(\boldsymbol{Y}_l, 2), 1)|^2$. Afterwards, we obtain the initial estimates for (τ, ν) as the argument that maximizes $\boldsymbol{Y}_{\tau,\nu}$. Note that since the range-Doppler map is quantized, one should perform fine tuning for better approximation. Therefore, in our application, we first apply the aforementioned fast implementation and then perform gradient ascent over the objective function in (33) by employing the initial estimates.

4) Angle Estimation

Given delay-Doppler estimates $(\widehat{\tau}, \widehat{\nu})$, we now wish to estimate azimuth and elevation angles $\boldsymbol{\theta} = [\theta_{az}\ \theta_{el}]^{\mathsf{T}}$ from the observations (see (30), repeated RIS phase profiles). We find that

$$\boldsymbol{Y} = \alpha \boldsymbol{c}(\widehat{\tau}) \left[(\boldsymbol{g}_L(\boldsymbol{\theta}) \odot \boldsymbol{d}_L(\widehat{\nu})) \otimes (\boldsymbol{d}_{M/L}(\widehat{\nu})) \right]^{\mathsf{T}} + \boldsymbol{Z}. \quad (34)$$

Again, α can be solved in closed form, so that the ML estimator becomes

$$\widehat{\boldsymbol{\theta}} = \arg\max_{\boldsymbol{\theta}} \frac{\left| \boldsymbol{c}^{\mathsf{H}}(\widehat{\tau}) \boldsymbol{Y} \left((\boldsymbol{g}_L(\boldsymbol{\theta}) \odot \boldsymbol{d}_L(\widehat{\nu})) \otimes \boldsymbol{d}_{M/L}(\widehat{\nu}) \right)^* \right|^2}{\| \boldsymbol{g}_L(\boldsymbol{\theta}) \|^2}, \quad (35)$$

which involves a 2D search over $\boldsymbol{\theta}$.

5) Refinement and Target Detection

We use the estimates $\widehat{\tau}, \widehat{\nu}, \widehat{\boldsymbol{\theta}}$ to initialize a 4D gradient ascent on (21), after which we plug the refined estimates into the original GRLT expression in (21), which then becomes

$$\frac{\left| \boldsymbol{c}^{\mathsf{H}}(\widehat{\tau}) \boldsymbol{Y} \left(\boldsymbol{g}(\widehat{\boldsymbol{\theta}}) \odot \boldsymbol{d}(\widehat{\nu}) \right)^* \right|^2}{\left\| \boldsymbol{g}(\widehat{\boldsymbol{\theta}}) \odot \boldsymbol{d}(\widehat{\nu}) \right\|^2} \underset{\mathcal{H}_0}{\overset{\mathcal{H}_1}{\gtrless}} \gamma . \quad (36)$$

IV. SIMULATION RESULTS

A. Scenario and Parameters

In the simulation setup, the center of the RIS is located at the origin, pointing towards the z-axis. We consider a point target 10 m away from the RIS with angle $\boldsymbol{\theta} = (45°, 60°)$, corresponding to $\boldsymbol{p}_{\text{tgt}} = \begin{bmatrix} 3.5355 & 3.5355 & 8.6603 \end{bmatrix}^{\mathsf{T}}$ in Cartesian coordinates. The target has a velocity vector of $\boldsymbol{v} = [30, 0, 30]$ m/s, which results in a relative speed of $\nu = -36.59$ m/s with respect to the RIS. The BS is located at $\boldsymbol{p}_{\text{BS}} = \begin{bmatrix} -3.0618 & 3.0618 & 2.5 \end{bmatrix}^{\mathsf{T}}$, 5 m away from the RIS with angle $\boldsymbol{\theta}^{\text{br}} = (135°, 30°)$. We generate RIS phase profiles to scan the region behind the obstacle (see Fig. 1), which is a quarter sphere. In other words, we create equally spaced angular beams in the region of $\theta_{\text{az}} \in [-90°, 90°]$ and $\theta_{\text{el}} \in [0°, 90°)$. In addition, $\lambda = 1.07\,\text{cm}$, $\sigma_{\text{RCS}} = 2\,\text{m}^2$, $N_{\text{RIS}} = 21 \times 21$, RIS element spacing $\lambda/4$, $G_b = 18.06\,\text{dB}$, $G = 0\,\text{dB}$, $N = 1024$ subcarriers with spacing $\Delta_f = 120\,\text{kHz}$ and $M = 1120$ symbols. The noise power spectral density is $N_0 = -174\,\text{dBm/Hz}$ and the receiver noise figure is 8 dB.

We vary the BS transmit power P_t and the number of RIS phase repetitions M/L for the considered scenario and perform the following analyses. We run 1000 Monte-Carlo tests for a given P_t and M/L to evaluate the performance of the proposed algorithm (termed 'Joint') in Sec. III-B. To study detection performance, we also need the probability of false alarms. Therefore, we perform the same procedure for noise-only signals with the same number of tests. As a benchmark, we consider an estimator that ignores the Doppler (denoted by 'DI' for Doppler-ignorant), similar to the studies [8]–[10]. The DI estimator is similar to the proposed estimator, but simply assumes $\nu = 0$.

B. Results and Discussion

To evaluate the performance of the proposed joint estimator, we calculate the RMSE based on Monte Carlo trials and compare it with the CRB. The results for range, Doppler, azimuth, and elevation are given in Figs. 2–5.
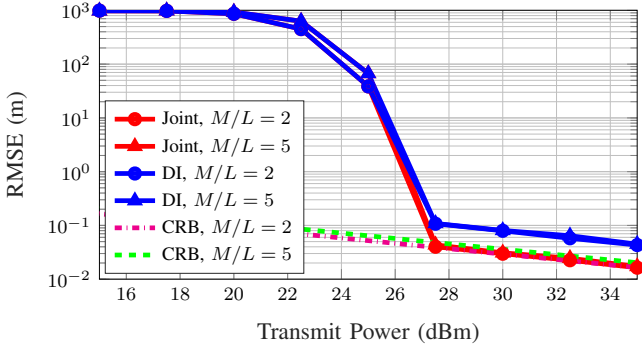
Fig. 2. RMSE of range estimation of joint and Doppler-ignorant (DI) estimator for $M/L = 2$ and $M/L = 5$ with CRB comparison.
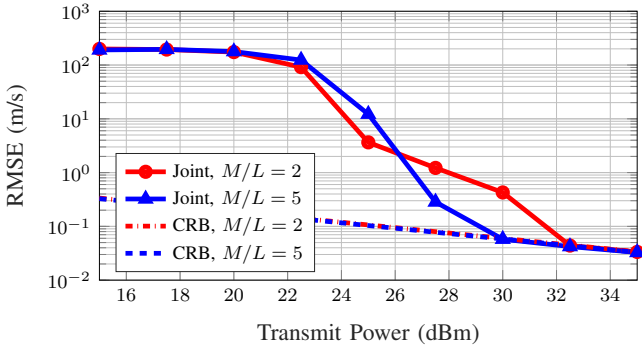

Fig. 3. RMSE of Doppler velocity estimation for $M/L = 2$ and $M/L = 5$ with CRB comparison.
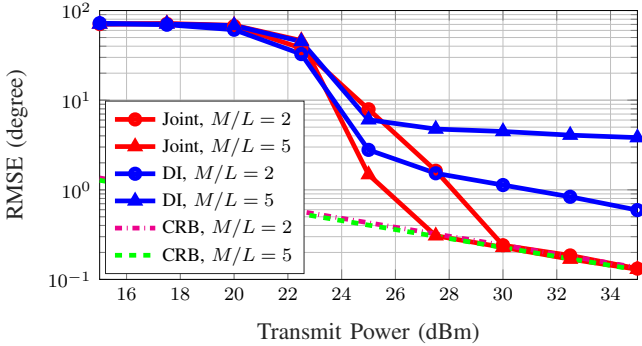

Fig. 4. RMSE of azimuth estimation of joint and Doppler-ignorant (DI) estimator for $M/L = 2$ and $M/L = 5$ with CRB comparison.
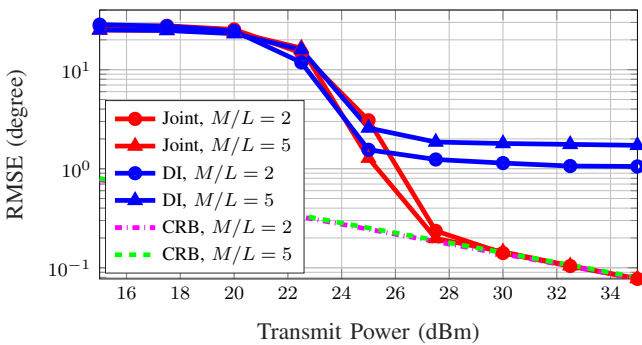

Fig. 5. RMSE of elevation estimation of joint and Doppler-ignorant (DI) estimator for $M/L = 2$ and $M/L = 5$ with CRB comparison.
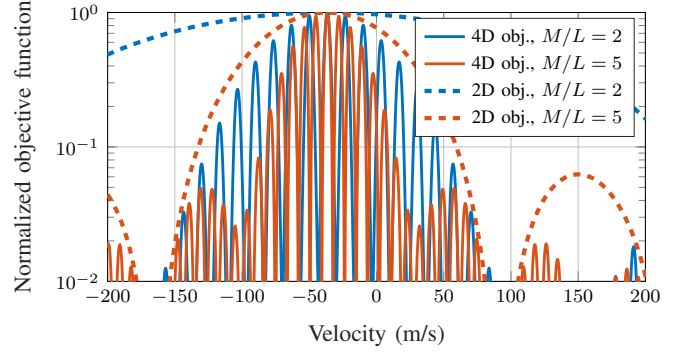

Fig. 6. Doppler velocity cut of objective function comparison between $M/L = 2$ and $M/L = 5$ and for objectives of (33) and (21). The other parameters are chosen as the exact target values.

1) Analysis of the Joint Estimator

It is clear that the proposed joint estimator shows a waterfall behavior and converges to the CRBs at high SNR, as expected. We see that the RMSE of the range behaves similarly for both $M/L = 2$ and $M/L = 5$. This is because the frequency-domain steering vector remains unaffected by RIS phase profiles. However, for Doppler and angle estimation, we observe that the RMSE for $M/L = 2$ converges to the CRB later than that for $M/L = 5$ in Figs. 3–5. This results from the nature of our estimator and can be explained by contrasting the original 4D objective functions (21) for the studied M/L values, obtained by the repetitive RIS phase profiles. The Doppler cuts of both 4D and 2D objective functions (21) and (33) are shown in Fig. 6 for different M/L. The 4D objective function has several local maxima that are closer and has smaller amplitude when M/L is higher. In other words, the sidelobes are higher and are at a larger distance when M/L is smaller. Hence, the other local maxima can exceed the main lobe in the presence of noise, and the estimates can converge to these points, resulting in some outliers, hence, large RMSEs.

2) Comparison with Doppler-Ignorant Approach

When applying the DI estimator, we see that range estimation in Fig. 2 is slightly degraded, due to biases induced by the Doppler. On the other hand, the RMSE of angle estimation in Fig. 4–5 shows a different trend and is more severely affected by the Doppler effect. This is due to angle-Doppler coupling, as both parameters are estimated by exploiting phase variations across time. When we compare the impact of M/L, the joint and Doppler-ignorant algorithms show different trends: joint estimation benefits from larger M/L, while Doppler-ignorant estimator is better at smaller M/L. Normally, it is expected that the performance of angle estimation would be enhanced for smaller M/L since we have more degrees of freedom (i.e., more diversity in RIS phase profiles), as in the case of the DI estimator. However, in Figs. 4–5, we have the opposite situation for the joint estimator since the angle error is affected by the error of Doppler estimation, which is shown in Fig. 3. It is observed that for high transmit powers, the Doppler estimation error is higher for $M/L = 2$. This is expected since for $M/L = 2$, the 4D objective function has higher sidelobes at larger distances as shown in Fig. 6. Therefore, the joint estimator leads to larger RMSEs on angle estimation for smaller M/L, resulting from the poor
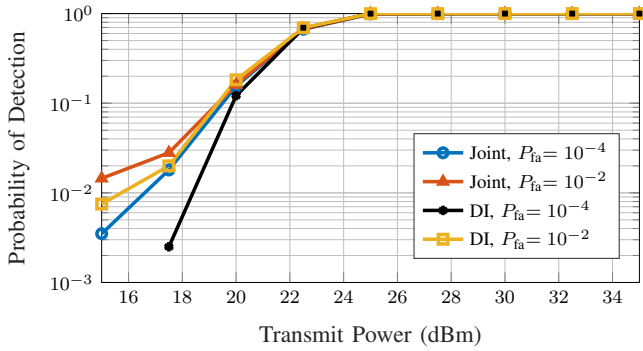
Fig. 7. Probability of detection versus transmit power for two different values of probability of false alarm.

Doppler estimation in (33) (which in turn deteriorates the angle estimation performance in (35) and affects the initialization point of 4D gradient ascent in (36)).

3) Detection Performance

Besides the estimation performance, we investigate the detection performance with respect to the transmit power for several false alarm rates, which is shown in Fig. 7. For a specified false alarm rate, we choose a threshold that ensures the same false alarm rate on the noise-only measurements. We observe that the detection performance is around one for transmit powers higher than 25 dBm. Additionally, it is seen that the joint estimator outperforms the Doppler ignorant one. Hence, we can conclude that it is crucial to account for the Doppler effect.

V. Conclusion

In this work, we addressed the time-domain coupling of Doppler-angle in an NLoS RIS-aided monostatic sensing scenario. To solve the coupling, we designed repetitive RIS phase profiles. Using the repetitive RIS phase profiles, we provided a low-complexity target parameter estimator that estimates delay, Doppler, and angles. Then, we derived the GLRT for target detection. We generated a simulation environment for a specified single-target case to analyze its performance. We evaluated the RMSE performance of the proposed GLRT-based low-complexity estimator and demonstrated its superior performance over the state-of-the-art Doppler-ignorant baseline. In addition, the detection performance was investigated to show that with higher transmit powers, we can detect the presence of the target with a reasonable false alarm rate. Future research will focus on multi-target scenarios.

References

[1] Q. Wu *et al.*, "Intelligent reflecting surface-aided wireless communications: A tutorial," *IEEE Transactions on Communications*, vol. 69, no. 5, pp. 3313–3351, 2021.

[2] Z. Chen *et al.*, "Intelligent reflecting surface assisted terahertz communications toward 6G," *IEEE Wireless Communications*, vol. 28, no. 6, pp. 110–117, 2021.

[3] E. C. Strinati *et al.*, "Reconfigurable, intelligent, and sustainable wireless environments for 6G smart connectivity," *IEEE Communications Magazine*, vol. 59, no. 10, pp. 99–105, 2021.

[4] R. Liu *et al.*, "Integrated sensing and communication with reconfigurable intelligent surfaces: Opportunities, applications, and future directions," *IEEE Wireless Communications*, vol. 30, no. 1, pp. 50–57, 2023.

[5] S. P. Chepuri *et al.*, "Integrated sensing and communications with reconfigurable intelligent surfaces: From signal modeling to processing," *IEEE Signal Processing Magazine*, vol. 40, no. 6, pp. 41–62, 2023.

[6] F. Liu *et al.*, "Integrated sensing and communications: Toward dual-functional wireless networks for 6G and beyond," *IEEE Journal on Selected Areas in Communications*, vol. 40, no. 6, pp. 1728–1767, 2022.

[7] S. P. Chepuri *et al.*, "Integrated sensing and communications with reconfigurable intelligent surfaces: From signal modeling to processing," *IEEE Signal Processing Magazine*, vol. 40, no. 6, pp. 41–62, 2023.

[8] R. S. Prasobh Sankar *et al.*, "Joint communication and radar sensing with reconfigurable intelligent surfaces," in *2021 IEEE 22nd International Workshop on Signal Processing Advances in Wireless Communications (SPAWC)*, 2021, pp. 471–475.

[9] H. Zhang *et al.*, "Metaradar: Multi-target detection for reconfigurable intelligent surface aided radar systems," *IEEE Transactions on Wireless Communications*, vol. 21, no. 9, pp. 6994–7010, 2022.

[10] S. Buzzi *et al.*, "Foundations of MIMO radar detection aided by reconfigurable intelligent surfaces," *IEEE Transactions on Signal Processing*, vol. 70, pp. 1749–1763, 2022.

[11] W. Lu *et al.*, "Target detection in intelligent reflecting surface aided distributed MIMO radar systems," *IEEE Sensors Letters*, vol. 5, no. 3, pp. 1–4, 2021.

[12] H. Kim *et al.*, "RIS-enabled and access-point-free simultaneous radio localization and mapping," *IEEE Transactions on Wireless Communications*, pp. 1–1, 2023.

[13] R. P. Sankar *et al.*, "Beamforming in integrated sensing and communication systems with reconfigurable intelligent surfaces," *IEEE Transactions on Wireless Communications*, pp. 1–1, 2023.

[14] R. Liu *et al.*, "Joint transmit waveform and passive beamforming design for RIS-aided DFRC systems," *IEEE Journal of Selected Topics in Signal Processing*, vol. 16, no. 5, pp. 995–1010, 2022.

[15] X. Song *et al.*, "Intelligent reflecting surface enabled sensing: Cramér-Rao bound optimization," *IEEE Transactions on Signal Processing*, vol. 71, pp. 2011–2026, 2023.

[16] Z. Esmaeilbeig *et al.*, "Cramér–Rao lower bound optimization for hidden moving target sensing via multi-IRS-aided radar," *IEEE Signal Processing Letters*, vol. 29, pp. 2422–2426, 2022.

[17] A. Aubry *et al.*, "Reconfigurable intelligent surfaces for N-LOS Radar surveillance," *IEEE Transactions on Vehicular Technology*, vol. 70, no. 10, pp. 10 735–10 749, 2021.

[18] S. Buzzi *et al.*, "RIS-aided monostatic MIMO radar with co-located antennas," in *ICASSP 2022 - 2022 IEEE International Conference on Acoustics, Speech and Signal Processing (ICASSP)*, 2022, pp. 4998–5002.

[19] E. Björnson *et al.*, "Reconfigurable intelligent surfaces: A signal processing perspective with wireless applications," *IEEE Signal Processing Magazine*, vol. 39, no. 2, pp. 135–158, 2022.

[20] E. Grossi *et al.*, "Radar target detection and localization aided by an active reconfigurable intelligent surface," *IEEE Signal Processing Letters*, pp. 1–5, 2023.

[21] X. Shao *et al.*, "Target sensing with intelligent reflecting surface: Architecture and performance," *IEEE Journal on Selected Areas in Communications*, vol. 40, no. 7, pp. 2070–2084, 2022.

[22] Z. Esmaeilbeig *et al.*, "IRS-aided radar: Enhanced target parameter estimation via intelligent reflecting surfaces," in *2022 IEEE 12th Sensor Array and Multichannel Signal Processing Workshop (SAM)*, 2022, pp. 286–290.

[23] S. Buzzi *et al.*, "Radar target detection aided by reconfigurable intelligent surfaces," *IEEE Signal Processing Letters*, vol. 28, pp. 1315–1319, 2021.

[24] Z. Xing *et al.*, "Joint active and passive beamforming design for reconfigurable intelligent surface enabled integrated sensing and communication," *IEEE Transactions on Communications*, 2023.

[25] T. Wei *et al.*, "Multi-IRS-aided Doppler-tolerant wideband DFRC system," *IEEE Transactions on Communications*, pp. 1–1, 2023.

[26] Z. Esmaeilbeig *et al.*, "Moving target detection via multi-IRS-aided OFDM radar," in *2023 IEEE Radar Conference (RadarConf23)*, 2023, pp. 1–6.

[27] K. Keykhosravi *et al.*, "SISO RIS-enabled joint 3D downlink localization and synchronization," in *ICC 2021 - IEEE International Conference on Communications*, 2021, pp. 1–6.

[28] A. B. Baral *et al.*, "Joint doppler frequency and direction of arrival estimation for TDM MIMO automotive radars," *IEEE Journal of Selected Topics in Signal Processing*, vol. 15, no. 4, pp. 980–995, 2021.

[29] S. P. Chepuri *et al.*, "Integrated sensing and communications with reconfigurable intelligent surfaces," *arXiv preprint arXiv:2211.01003*, 2022.

[30] X. Shao *et al.*, "Intelligent reflecting surface aided wireless sensing: Applications and design issues," *arXiv preprint arXiv:2302.05864*, 2023.

[31] R. F. Tigrek *et al.*, "OFDM signals as the radar waveform to solve Doppler ambiguity," *IEEE Transactions on Aerospace and Electronic Systems*, vol. 48, no. 1, pp. 130–143, Jan. 2012.

[32] M. Braun, "OFDM radar algorithms in mobile communication networks," Phd Dissertation, Karlsruhe Institute of Technology, 2014.

[33] K. V. Mishra *et al.*, "Toward millimeter-wave joint radar communications: A signal processing perspective," *IEEE Signal Processing Magazine*, vol. 36, no. 5, pp. 100–114, Sep. 2019.

[34] M. F. Keskin *et al.*, "MIMO-OFDM joint radar-communications: Is ICI friend or foe?" *IEEE Journal of Selected Topics in Signal Processing*, vol. 15, no. 6, pp. 1393–1408, 2021.

[35] D. Dardari *et al.*, "LOS/NLOS near-field localization with a large reconfigurable intelligent surface," *IEEE Transactions on Wireless Communications*, vol. 21, no. 6, pp. 4282–4294, 2022.

[36] H. L. Van Trees, *Optimum Array Processing: Part IV of Detection, Estimation, and Modulation Theory*. John Wiley & Sons, 2002.

[37] M. F. Keskin *et al.*, "Limited feedforward waveform design for OFDM dual-functional radar-communications," *IEEE Transactions on Signal Processing*, vol. 69, pp. 2955–2970, 2021.